

Modifications for an explicit algebraic stress model

M. M. Rahman^{*,1}, P. Rautahaimo and T. Siikonen

*Laboratory of Applied Thermodynamics, Helsinki University of Technology, Sähkömiehentie 4,
FIN-02015 HUT, Finland*

SUMMARY

An extension of the explicit algebraic stress model, developed by Gatski and Speziale [Gatski TB, Speziale CG. On the explicit algebraic stress models for complex turbulent flows. *Journal of Fluid Mechanics* 1993; 254: 59–78] is proposed. The extension implicates some essential characteristics of second-order closure models. The strain-dependent coefficients are modified, resulting in an alleviation of the numerical instabilities involved in the model. A new near-wall damping function f_μ in the eddy viscosity relation is introduced. To enhance dissipation in near-wall regions, the model constant $C_{\epsilon 1}$ is modified and an extra positive source term is included in the dissipation equation. In addition, a realizable time scale is incorporated to remove the wall singularity. Computed results show that the modified Gatski–Speziale (MGS) model predictions are in better agreement with the direct numerical simulation (DNS) and experimental data than those of the original Gatski–Speziale (OGS) model. Copyright © 2001 John Wiley & Sons, Ltd.

KEY WORDS: anisotropy of turbulence; damping function; turbulence model

1. INTRODUCTION

Second-order closure models of turbulence, which are based on the Reynolds stress transport equation, entangle the history and non-local effects automatically. Basically, they are formulated to describe complex turbulent flows where there are significant departures from equilibrium. With the help of the equilibrium hypothesis, Rodi [1] proposed an idea of obtaining the algebraic stress model (ASM) from the second-order closures. Physically, two assumptions are made in the algebraic Reynolds stress closures: the difference between the convection and diffusion terms in the Reynolds stress equation is proportional to the corresponding difference in the turbulent kinetic energy equation, and the Reynolds stress anisotropy b_{ij} is constant

* Correspondence to: Laboratory of Applied Thermodynamics, Helsinki University of Technology, Sähkömiehentie 4, FIN-02015 HUT, Espoo, Finland.

¹ E-mail: mizanur.rahman@hut.fi

along a streamline. It provides algebraic equations without solving the differential equations for the Reynolds stresses.

Invoking the same equilibrium hypothesis as Rodi, Pope [2] developed a methodology to procure an explicit relation for the Reynolds stress tensor from the implicit algebraic stress model (which Rodi obtained from the model of Launder *et al.* [3]) by using a tensorial polynomial expansion in the integrity basis. Gatski and Speziale [4] used this method to derive an explicit algebraic stress equation for two- and three-dimensional turbulent flows. In order to generalize the results, the algebraic stress representation is applied to the general class of pressure–strain correlation models [5], which are linear in the anisotropic tensor. After regularization, an anisotropic eddy viscosity model with strain-dependent coefficients is achieved, which has been referred to as an explicit ASM. Unambiguously, the explicit model extends the ability of the two-equation models to account for non-equilibrium and anisotropic effects. However, the model shows evidence of numerical instability when the flow is far from equilibrium [6]. The reason is that the ASM is more susceptible to the rotational strains.

In the present study, an extended version of the original Gatski–Speziale (OGS) model is constructed. Some modifications for the coefficients that depend non-linearly on both the rotational and irrotational strains are proposed based on the realizability constraints, i.e., the positivity of the normal Reynolds stresses and Schwarz’s inequality between turbulent velocity correlations. Consequently, the strain-dependent sensitivity of the model is mitigated and a notable improvement in the numerical stability is attained. In near-wall regions, the ‘anisotropic production’ in the ϵ -equation is accounted for substantially by modifying the model constant $C_{\epsilon 1}$ and adding a secondary source term. Furthermore, the wall singularity is removed by using a physically appropriate time scale that never falls below the Kolmogorov time scale $\sqrt{\nu/\epsilon}$, representing the near-wall turbulent phenomena. A near-wall eddy viscosity damping function f_μ is introduced, which reaches the upper limit value of unity in the logarithmic layer.

The performance of the modified Gatski–Speziale (MGS) model is evaluated by calculating some well-acquainted turbulent flows, consisting of fully developed channel flows, a flat-plate boundary layer flow with zero pressure gradient, a backward-facing step flow, and heat transfer coefficients for semi-confined impinging slot and round jets respectively.

2. TURBULENCE MODELING

The two-dimensional Reynolds-averaged Navier–Stokes (RANS) equations, including the equations for the kinetic energy k and dissipation ϵ , can be written in the following form:

$$\frac{\partial U}{\partial t} + \frac{\partial(F - F_v)}{\partial x} + \frac{\partial(G - G_v)}{\partial y} = Q \quad (1)$$

where $U = (\rho, \rho u, \rho v, E, \rho k, \rho \epsilon)^T$. The inviscid fluxes are

$$F = \begin{pmatrix} \rho u \\ \rho u^2 + p + \frac{2}{3} \rho k \\ \rho uv \\ u \left(E + p + \frac{2}{3} \rho k \right) \\ \rho uk \\ \rho u \epsilon \end{pmatrix}, \quad G = \begin{pmatrix} \rho v \\ \rho vu \\ \rho v^2 + p + \frac{2}{3} \rho k \\ v \left(E + p + \frac{2}{3} \rho k \right) \\ \rho vk \\ \rho v \epsilon \end{pmatrix} \quad (2)$$

Here ρ is the density and p is the pressure. The total internal energy is defined as

$$E = \rho e + \frac{\rho \vec{V} \cdot \vec{V}}{2} + \rho k \quad (3)$$

where e is the specific internal energy and $\vec{V} = u\vec{i} + v\vec{j}$ is the velocity. The viscous fluxes are

$$F_v = \begin{pmatrix} 0 \\ \tau_{xx} + \frac{2}{3} \rho k \\ \tau_{xy} \\ u\tau_{xx} + v\tau_{xy} - q_x \\ \mu_k \frac{\partial k}{\partial x} \\ \mu_\epsilon \frac{\partial \epsilon}{\partial x} \end{pmatrix}, \quad G_v = \begin{pmatrix} 0 \\ \tau_{xy} \\ \tau_{yy} + \frac{2}{3} \rho k \\ u\tau_{xy} + v\tau_{yy} - q_y \\ \mu_k \frac{\partial k}{\partial y} \\ \mu_\epsilon \frac{\partial \epsilon}{\partial y} \end{pmatrix} \quad (4)$$

and the viscous stress tensor can be given as

$$\tau_{ij} = \mu \left(\frac{\partial u_j}{\partial x_i} + \frac{\partial u_i}{\partial x_j} - \frac{2}{3} (\nabla \cdot \vec{V}) \delta_{ij} \right) - \rho \overline{u_i u_j} \quad (5)$$

where μ is the laminar viscosity and $\overline{\rho u_i u_j}$ are the Reynolds stresses. The heat flux is calculated from

$$\vec{q} = -(k + k_T) \nabla T = - \left(\mu \frac{c_p}{Pr} + \mu_T \frac{c_p}{Pr_T} \right) \nabla T \quad (6)$$

where μ_T is the coefficient of turbulent viscosity, k and k_T are the laminar and turbulent thermal conductivity coefficients, and Pr and Pr_T represent the laminar and turbulent Prandtl numbers respectively. Clearly, the turbulent part of the total heat flux is estimated using the Boussinesq approximation. The diffusion of turbulence is modeled as

$$\mu_k \nabla k = \left(\mu + \frac{\mu_T}{\sigma_k} \right) \nabla k, \quad \mu_\epsilon \nabla \epsilon = \left(\mu + \frac{\mu_T}{\sigma_\epsilon} \right) \nabla \epsilon \tag{7}$$

where σ_k and σ_ϵ are the appropriate empirical constants. The source term Q for the k and ϵ equations can be written as

$$Q = \left[\begin{array}{c} \rho P - \rho \epsilon \\ C_{\epsilon 1} \frac{\rho \epsilon}{k} P - C_{\epsilon 2} f_2 \frac{\rho \epsilon^2}{k} + E \end{array} \right] \tag{8}$$

where the turbulence production term $P = \overline{u_i u_j} (\partial u_i / \partial x_j)$. The eddy viscosity is evaluated as

$$\mu_T = C_\mu f_\mu \rho \frac{k^2}{\epsilon} \tag{9}$$

Table I summarizes functions and constants for different turbulence models. The friction velocity u_τ , dimensionless distance y^+ and different Reynolds numbers associated with the turbulence modeling are defined as

$$Re_T = \frac{\rho k^2}{\mu \dot{\epsilon}}, \quad Re_y = \frac{\rho \sqrt{k} y_n}{\mu}, \quad y^+ = \frac{\rho y_n u_\tau}{\mu}, \quad u_\tau = \sqrt{\tau_w / \rho} \tag{10}$$

where y_n is the normal distance from the wall and τ_w represents the wall shear stress. The modeling of $\overline{\rho u_i u_j}$ in the explicit ASM and associated relevant aspects are discussed in some detail in subsequent sections.

Table I. Functions and constants.

Model	D	ϵ_w - B.C.	$C_{\epsilon 1}$	$C_{\epsilon 2}$	Pr_T	σ_k	σ_ϵ	C_μ
OGS	0.0	$2\nu(\partial \sqrt{k} / \partial y_n)^2$	1.44	1.83	0.9	1.0	1.4	0.088
MGS	0.0	$2\nu(k/y_n^2)$	(27)	1.83	0.9	1.0	1.4	(20)
		f_μ f_2	E					
OGS	1.0	$1.0 - \exp(-Re_y/12.5)$	0.0					
MGS	(26)	1.0	(31)					

Figures in parentheses represent Equation numbers.

2.1. Original explicit ASM

The explicit solution to the Reynolds-stress tensor $\overline{\rho u_i u_j}$, obtained by Gatski and Speziale, constitutes an anisotropic eddy viscosity model with strain-dependent coefficients. For two-dimensional mean turbulent flows, the non-linear constitutive equation takes a simplified form

$$\begin{aligned} \overline{\rho u_i u_j} = & \frac{2}{3} \rho k \delta_{ij} - 2C_\mu \rho \frac{k^2}{\epsilon} \left[\left(S_{ij} - \frac{1}{3} S_{kk} \delta_{ij} \right) + \alpha_4 \frac{k}{\epsilon} (S_{ik} W_{kj} + S_{jk} W_{ki}) \right. \\ & \left. - \alpha_5 \frac{k}{\epsilon} \left(S_{ik} S_{kj} - \frac{1}{3} S_{kl} S_{kl} \delta_{ij} \right) \right] \end{aligned} \tag{11}$$

with

$$C_\mu = \frac{3(1 + \eta^2)\alpha_1}{3 + \eta^2 + 6\xi^2\eta^2 + 6\xi^2} \tag{12}$$

$$\eta^2 = \alpha_2 \left(\frac{Sk}{\epsilon} \right)^2, \quad \xi^2 = \alpha_3 \left(\frac{Wk}{\epsilon} \right)^2 \tag{13}$$

where Sk/ϵ and Wk/ϵ represent the shear and vorticity parameters respectively; $S = \sqrt{2S_{ij}S_{ij}}$ and $W = \sqrt{2W_{ij}W_{ij}}$. The mean strain rate and mean vorticity tensors S_{ij} and W_{ij} are defined as

$$S_{ij} = \frac{1}{2} \left(\frac{\partial u_i}{\partial x_j} + \frac{\partial u_j}{\partial x_i} \right), \quad W_{ij} = \frac{1}{2} \left(\frac{\partial u_i}{\partial x_j} - \frac{\partial u_j}{\partial x_i} \right) \tag{14}$$

The coefficients $\alpha_1 - \alpha_5$ associated with Equations (11)–(13) are given by

$$\begin{aligned} \alpha_1 = & \left(\frac{4}{3} - C_2 \right) \frac{g}{2}, \quad \alpha_2 = (2 - C_3)^2 \frac{g^2}{8}, \quad \alpha_3 = (2 - C_4)^2 \frac{g^2}{8}, \quad \alpha_4 = (2 - C_4) \frac{g}{2}, \\ \alpha_5 = & (2 - C_3)g; \quad g = \left(\frac{C_1}{2} + \frac{P}{\epsilon} - 1 \right)^{-1} \end{aligned} \tag{15}$$

The pressure–strain correlation model of Speziale *et al.* [7] is considered herein so that $C_1 - C_4$ become

$$C_1 = 3.4 + 1.80 \frac{P}{\epsilon}, \quad C_2 = \frac{4}{5} - 1.30 \Pi_b^{1/2}, \quad C_3 = 1.25, \quad C_4 = 0.40 \tag{16}$$

where $\Pi_b = b_{ij}b_{ij}$ and the anisotropy of the Reynolds stress b_{ij} is defined as

$$b_{ij} = \frac{\overline{u_i u_j} - \frac{2}{3} k \delta_{ij}}{2k} \tag{17}$$

For homogeneous turbulent flows that are in equilibrium, Π_b and P/ϵ attain constant values, so that $\Pi_b \approx 0.11$ and $P/\epsilon = (C_{e2} - 1)/(C_{e1} - 1) \approx 1.88$. These values are set in Equations (15) and (16) to calculate inhomogeneous flows. The function f_2 given in Table I removes the singularity of the dissipation equation at the wall [6]. The model can be integrated to the wall without adding a damping to the eddy viscosity, since the strain-dependent coefficient C_μ in the eddy viscosity equation provides natural damping as the wall is approached.

2.2. Modified explicit ASM

Obviously, the explicit algebraic stress model augments the capacity of the two-equation models to account for non-equilibrium effects through the coefficient C_μ . Unfortunately, the OGS model exhibits numerical instability in the context of the algebraic stress model when the flow is far from equilibrium. The reason is that the model responds more sensitively to the strain-dependent coefficients (i.e., rotational strains). To avoid a numerical problem, a modified form of C_μ is proposed in Reference [8]

$$C_\mu \approx \frac{\alpha_1}{1 + 4\eta^2 + \xi^2} \quad (18)$$

Note that Equation (18) is equivalent to Equation (12) for the homogeneous shear flow, which is characterized by

$$S_{12} = \frac{S}{2} = S_{21}, \quad W_{12} = \frac{S}{2} = -W_{21}, \quad S = \frac{\partial u}{\partial y} \quad (19)$$

Figure 1, which shows the distribution of C_μ as a function of Sk/ϵ , bears evidence for this. The proposed modification reduces the strain-dependent sensitivity and numerical difficulties to some extent. An alternative regularized form of C_μ is used by Abid *et al.* [7] in aerodynamic flow computations. The formulation is synonymous to Equation (12) to the order η^6 and ξ^6 ,

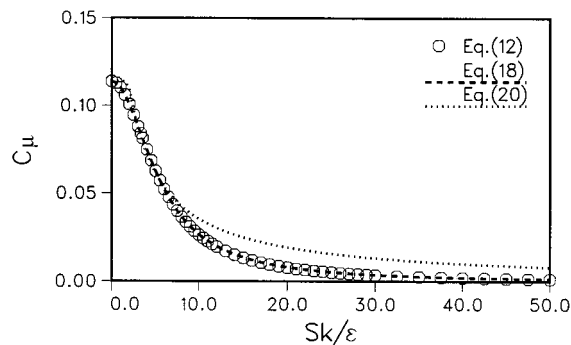


Figure 1. Distribution of C_μ as a function of the shear parameter Sk/ϵ .

since it does not discernibly alter the value of C_μ near equilibrium conditions, but limits C_μ to a non-zero value ($0.2\alpha_1$) for high values of η and ξ to preclude numerical instabilities. However, to maintain the relevant aspects of the MGS model, the coefficient C_μ cannot be a constant.

As is observed from Figure 1, the coefficient C_μ (and therefore the turbulent viscosity) decreases as the parameter Sk/ϵ increases. Distinguishably, C_μ in Equation (18) has still the tendency to damp out the eddy viscosity at higher values of Sk/ϵ . To root this situation out, a plausible formulation is devised following Reference [7] as

$$C_\mu^* = \min \left[\alpha_1, \frac{2\alpha_1}{1 + 3\sqrt{4\eta^2 + \xi^2}} \right] \tag{20}$$

Actually, Equation (12) or (18) is used to calibrate the coefficient C_μ^* , focusing attention toward the homogeneous shear flow (Figure 1). The modified C_μ^* is reduced significantly by the shear parameter, i.e., the mean strain rate is maintained at a such level that could mimic the complex turbulent flows.

The physically necessary conditions for a turbulence model are the realizability conditions that may be defined as [5]

$$\overline{u_i^2} \geq 0, \quad \frac{\overline{u_i u_i^2}}{\overline{u_i^2} \overline{u_j^2}} \leq 1 \tag{21}$$

In order to make the eddy viscosity model realizable, an alternative form of the coefficient g associated with α_4 and α_5 , is considered

$$g^* = \frac{1}{1 + 3(4\eta^2 + \xi^2)} \tag{22}$$

Obviously, the coefficient g^* is capable of responding to both the shear and vorticity dominated flows that are far from equilibrium. Note that Equation (22) gives $g^* \approx 0.22$ for Tavoularis and Corrsin's [9] homogeneous shear flow at $Sk/\epsilon = 6.0$, which is very close to the value of g ($= 0.233$) used in Equation (15).

The non-linear constitutive equation, combined with the above-mentioned modifications is reconstructed as

$$\begin{aligned} \overline{\rho u_i u_j} = & \frac{2}{3} \rho k \delta_{ij} - 2\mu_T \left[\left(S_{ij} - \frac{1}{3} S_{kk} \delta_{ij} \right) + \alpha_4 T_t (S_{ik} W_{kj} + S_{jk} W_{ki}) \right. \\ & \left. - \alpha_5 T_t \left(S_{ik} S_{kj} - \frac{1}{3} S_{kl} S_{kl} \delta_{ij} \right) \right] \end{aligned} \tag{23}$$

with

$$\alpha_4 = (2 - C_4)g^*/2, \quad \alpha_5 = (2 - C_3)g^*, \quad \mu_T = C_{\mu}^* f_\mu \rho k T_t, \quad T_t = \max(k/\epsilon, C_T \sqrt{\nu/\epsilon}) \tag{24}$$

where the coefficient g^* is given by Equation (22). Other constants are the same as those employed in the OGS model. The realizable time scale T_t warrants that the eddy time scale never falls below the Kolmogorov (dissipative eddy) time scale $\sqrt{\nu/\epsilon}$, dominant in the immediate vicinity of the solid wall. This turbulence time scale prevents the singularity at $y_n = 0$ in the dissipation equation. Therefore, the source term Q of the ϵ -equation is recast as

$$Q = \frac{C_{\epsilon 1} \rho P - C_{\epsilon 2} \rho \epsilon}{T_t} + E \quad (25)$$

This approach has been previously devised by Durbin [10] and, in a different context, by Goldberg [11], and later adopted by others [12,13]. Nevertheless, the empirical constant C_T associated with the Kolmogorov time scale in Equation (24) induces an ‘arbitrariness’. The dissipative eddy time scale is activated when $y^+ < 5$ (this range is possibly extensible with an increase in C_T), and the turbulence models constructed so far have deemed values of C_T in the range of 1–6.

For the MGS model, $C_T = \sqrt{2}$ is used, which is estimated as follows [13]. In the viscous sub-layer, $k = y^2/(C_T^2 \nu/\epsilon)$, where the basic scale is the Kolmogorov time scale. Besides, the k -equation reduces to $\nu \partial^2 k / \partial y^2 = \epsilon$ as the wall is approached. Combining these relations provides $C_T = \sqrt{2}$.

The near-wall damping function f_μ for the eddy viscosity in Equation (24) is chosen as

$$f_\mu = \tanh[0.26(Re_y^{1.5}/Re_T)^{1.5}] \quad (26)$$

and is valid in the whole flow field, including the viscous sub-layer and the logarithmic layer. As shown in Figure 2(a), the proposed function approaches unity far from the wall, which indicates that the standard k - ϵ model form is recovered. The Reynolds number, $Re_\tau \equiv u_\tau \delta/\nu$, in the test calculations is based on the friction velocity u_τ and the channel half-width δ . In principle, the eddy viscosity confronts two major dynamic effects; the effect of wall proximity in the near-wall region through f_μ , and the non-equilibrium effect through the coefficient C_μ^* away from the wall.

When solving the full system of equations, the computed results show a tendency to underestimate the dissipation rate ϵ in near-wall flows. The reasons are exquisitely documented in References [14,15]. Various formulations have been developed to enhance dissipation in such situations [16–19]. In Reference [17], the non-dimensional parameter P/ϵ is used to increase the production of ϵ in the near-wall region: $C_{\epsilon 1}^* = 1.44(1 + a_1 P/\epsilon)$, with $a_1 = 0.1$ [1]. However, this procedure can cause numerical instability in more complex flows. In the present study, a replacement of this unstable term is explored as

$$C_{\epsilon 1} = 1.3 + \frac{C_\mu^*}{23} \max[(Sk/\epsilon)^2, (Wk/\epsilon)^2] \quad (27)$$

Figure 1 essentially reveals that C_μ^* in Equation (20) allows reasonable changes in $C_{\epsilon 1}$. The relation is designed such that $C_{\epsilon 1}$ takes the anisotropy of turbulence into account.

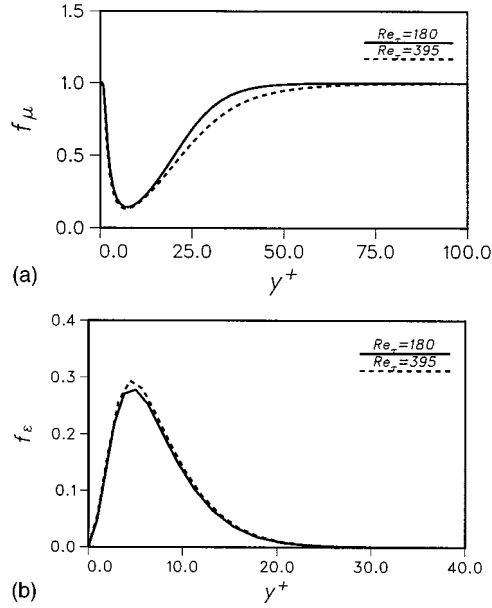


Figure 2. Variations of the damping functions with the wall distance in a channel flow.

The secondary source term E in Equation (25) is constructed in a manner so that its near-wall limit dissolves the corresponding non-zero destruction term in the ϵ -equation. Therefore, it follows that

$$E = C_{\epsilon 2} \rho \epsilon_w / (C_T \sqrt{\nu / \epsilon}) \tag{28}$$

where ϵ_w signifies the wall-dissipation rate and is equal to the viscous-diffusion rate [20]

$$\epsilon_w = 2A_\epsilon \nu \left(\frac{\partial u}{\partial y} \right)_w^2 \tag{29}$$

with

$$\left(\frac{\partial u}{\partial y} \right)_w^2 \approx 2S_{ij}S_{ij} = S^2$$

where A_ϵ ($\epsilon_w^+ / 2 = \nu \epsilon_w / 2u_\tau^4$) is a function of the Reynolds number. Experimental and DNS data of flat plate and channel flows indicate that $0.05 < A_\epsilon < 0.11$, with a preference for higher values at larger Reynolds numbers [20–23]. At the wall, C_μ^* (≈ 0.114) gets closer to the maximum limit of A_ϵ . It is more convenient to use C_μ^* instead of selected values for A_ϵ since

ϵ (as well as C_μ^*) varies very rapidly near the wall. Consequently, the above relations combine to yield

$$E = \frac{2C_{\epsilon 2} C_\mu^* \rho \sqrt{\nu \epsilon}}{C_T} S^2 \quad (30)$$

To reproduce the level of kinetic energy (and therefore the wall-dissipation rate, since it is dependent on k , see Table I) in the immediate vicinity of the wall, E must vanish at the wall. In addition, E must lose its influence outside the close proximity of the wall in order to recover the parent high-Reynolds number model. Therefore, a function must be devised so as to make E zero at the wall as well as far from the wall. Here, the form is adopted as

$$E = \frac{2C_{\epsilon 2} C_\mu^* \rho \sqrt{\nu \epsilon}}{C_T} S^2 f_\epsilon \quad (31)$$

with

$$f_\epsilon = \tanh(0.20\sqrt{Re_T}) \exp(-0.24\sqrt{R_k}) \quad (32)$$

where $R_k = K_T/\nu S$ and $K_T = \vec{V} \cdot \vec{V}/2 + k$. The constants associated with Equation (32) are tuned with the model based on well-studied flows considered hereinafter. According to Durbin's hypothesis, the mechanism conveyed through the function f_ϵ can be addressed as the 'kinematic wall blocking'. The distribution of f_ϵ as a function of the wall distance in a channel flow is shown in Figure 2(b). Remote from the wall, a gradual approach toward zero of E (becomes much smaller than the other terms in the ϵ -equation) is accelerated by both C_μ^* (natural damping) and f_ϵ (artificial damping). From the distributions of C_μ^* and f_ϵ in Figures 1 and 2(b) respectively; it seems that the effect of E is confined within the wall layer ($y^+ \leq 30$).

Using Equation (17), the Reynolds stress anisotropies in homogeneous shear flow can be derived from Equation (23) as

$$\begin{aligned} b_{11} &= \left(\frac{\alpha_4}{2} + \frac{\alpha_5}{12} \right) C_\mu^* \left(\frac{Sk}{\epsilon} \right)^2 \\ b_{22} &= \left(-\frac{\alpha_4}{2} + \frac{\alpha_5}{12} \right) C_\mu^* \left(\frac{Sk}{\epsilon} \right)^2 \\ b_{12} &= -\frac{C_\mu^* Sk}{2 \epsilon} \end{aligned} \quad (33)$$

Detailed comparisons of the anisotropies with the DNS and experimental data are shown in Table II for the channel flow of Kim [Personal communication 1990] in the inertial sub-layer at $Sk/\epsilon = 3.3$, and in Table III for the homogeneous shear flow of Tavoularis and Corrsin at $Sk/\epsilon = 6.0$ respectively. Clearly, the present and also the OGS models provide reasonable anisotropy of Reynolds stresses for both the boundary layer and homogeneous shear flows,

Table II. Anisotropy in the log layer of channel flow.

b_{ij}	DNS	Standard	OGS	MGS
b_{11}	0.175	0.0	0.099	0.198
b_{12}	-0.145	-0.149	-0.139	-0.134
b_{22}	-0.145	0.0	-0.072	-0.144

compared with the standard $k-\epsilon$ eddy viscosity model. Therefore, they are capable of predicting the turbulent-driven secondary flows. As can be seen from Table II, the predicted anisotropy (b_{11} and b_{22}) by the OGS model is weaker than that of the MGS model, which may result in a difference of accuracy.

Variations of the Reynolds stress anisotropies in the homogeneous shear flow are shown in Figure 3 as a function of the shear parameter Sk/ϵ . Noteworthy, in pure shear flows, the OGS model tends to exhibit improper behavior at higher values of Sk/ϵ , since the component b_{12} approaches zero as Sk/ϵ increases. The C_μ -distribution in Figure 1 also clarifies the unexpected consequences of the OGS model. On the contrary, the unusual feature of b_{12} is diminished in the MGS model. This improvement is mainly due to the behavior of C_μ^* in the MGS model. It is important to mention that the present model satisfies the realizability constraint in Equation (21), a clear demonstration of which is provided by Figure 3. However, experience shows that numerical formulations of the modeled equations do not exactly satisfy the strong form of realizability, i.e., a sufficient condition to guarantee the positivity in energy components, always.

3. SOLUTION METHOD

A cell-centered finite volume scheme together with an artificial compressibility approach [8] is employed to solve the flow equations. In the artificial compressibility method, the artificial compressibility is principally added to the derivative of density with respect to the pressure, influencing not only the continuity equation but also the other equations. The energy equation is not decoupled from the system of equations, which facilitates a uniform treatment for both the primitive and conservative variables. A fully upwinded second-order spatial differencing is applied to approximate the convective terms. Roe's [24] damping term is used to calculate the flux on the cell face. A diagonally dominant alternating direction implicit (DDADI) time integration method [25] is applied for the iterative solution of the discretized equations. A multigrid method is utilized for the acceleration of convergence [26]. The basic implementation

Table III. Anisotropy in the homogeneous shear flow.

b_{ij}	Experiment	Standard	OGS	MGS
b_{11}	0.202	0.0	0.203	0.196
b_{12}	-0.142	-0.273	-0.156	-0.160
b_{22}	-0.145	0.0	-0.148	-0.143

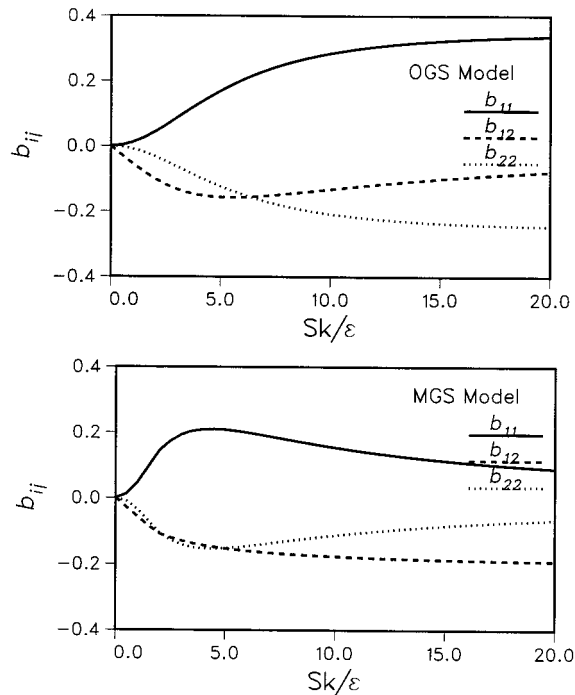


Figure 3. Anisotropy tensors as a function of the shear parameter Sk/ϵ .

of the artificial compressibility method and associated features are described in Reference [8,27,28].

4. RESULTS AND DISCUSSION

To ascertain the generality and efficacy of the MGS model, a few applications to two-dimensional turbulent flows are considered. Tested flows consist of fully developed channel flows, a flat plate boundary layer flow with zero pressure gradient, a backward-facing step flow, and heat transfer from semi-confined impinging slot and round jets. For a comparison purpose, a widely used low-Reynolds number $k-\epsilon$ model of Chien (CH) is considered [29]. Some calculations from the OGS model are also included. Note that for the OGS model, Equation (11) is solved in the framework of the $k-\epsilon$ formulation assuming a constant value for C_μ that Table I shows, in evaluating the turbulent diffusion (i.e., the traditional eddy viscosity concept) for k and ϵ equations as suggested by References [4,6]. Unfortunately, for the backward-facing step and jet impingement flows involving the flow separation and reattachment, the OGS model receives no convergence from the numerical method implemented herein. Probably, the numerical issue plays an influential role to cause divergence for the OGS model.

4.1. Channel flow

Computations are carried out for fully developed turbulent channel flows at $Re_\tau = 180$ and 395, for which turbulence quantities are attainable from the DNS data [22]. Calculations are conducted in the half-width of the channel, imposing periodic boundary conditions, except for the pressure, pertaining to the upstream and downstream boundaries. Computations involving a 48×32 non-uniform grid refinement for $Re_\tau = 180$ and 48×48 for $Re_\tau = 395$ are considered to be sufficiently accurate to describe the flow characteristics. For both cases, the length of the computational domain is 32δ , and the height of the first row of cells is located at $y^+ < 1.0$. Comparisons are made by plotting the results in the form of $u^+ = u/u_\tau$, $k^+ = k^+/u_\tau^2$, $\overline{uv}^+ = \overline{uv}/u_\tau^2$ and $\epsilon^+ = \nu\epsilon/u_\tau^4$ versus y^+ .

Figure 4 shows the velocity profiles for different models. Predictions of both the MGS and CH models agree well with the DNS data. The OGS model overestimates the mean velocity profile in the outer layer. Profiles of turbulent shear stresses are displayed in Figure 5. Agreement of the MGS model prediction with the DNS data seems to be almost perfect. As can be seen, both the OGS and CH models underpredict the shear stress at $Re_\tau = 180$ in the $y^+ > 20$ range.

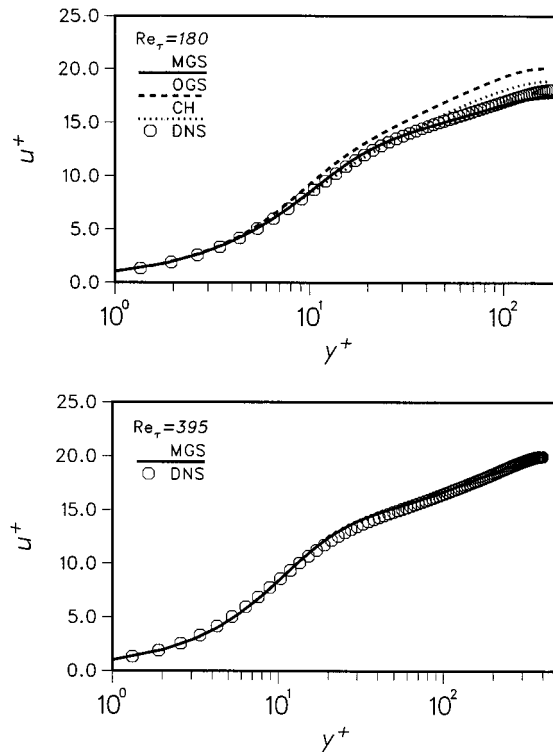


Figure 4. Mean velocity profiles of channel flow.

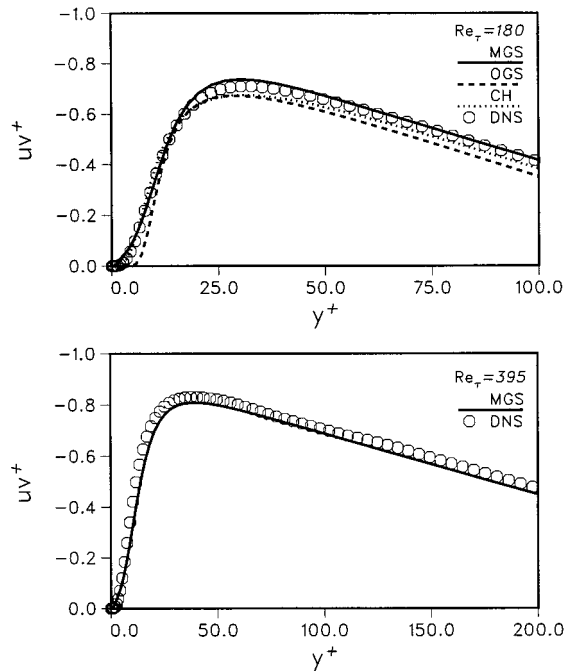


Figure 5. Shear stress profiles of channel flow.

Figure 6 portrays the k^+ -profiles as predicted by all models. As is evident, the MGS model gives some improvement in the prediction of k^+ compared with the OGS model. Actually, the eddy viscosity damping function f_μ plays a key role in the prediction of the turbulent kinetic energy which is introduced with the MGS model. The CH model predicts a peak at a slightly shifted location. The OGS model badly underestimates the value of k^+ in the near-wall region $0 \leq y^+ < 5$.

Figure 7 exhibits the profiles of ϵ^+ from the three computations. Note that the ϵ^+ calculated by the CH model is a reduced ϵ^+ (i.e., $\tilde{\epsilon}$), it has to go to zero at the wall. Surprisingly, the OGS model yields a low prediction for ϵ^+ in the inner region $0 \leq y^+ < 5$ and predicts a large maximum away from the wall, although it does not presume a zero value for ϵ at the wall. On the contrary, the MGS model provides a maximum ϵ^+ at the wall which is more in line with the experimental and DNS data.

4.2. Flat-plate boundary layer flow

The near-wall behavior of the turbulence model is checked by calculating the flow over a flat-plate with a high free-stream turbulence intensity. The test case is taken from 'ERCOFTAC' Fluid Dynamics Database WWW Services (<http://fluindigo.mech.surrey.ac.uk/>) preserved by P. Voke. Measurements down to $x = 1.495$ m, which corresponds to $Re_x \approx 94000$,

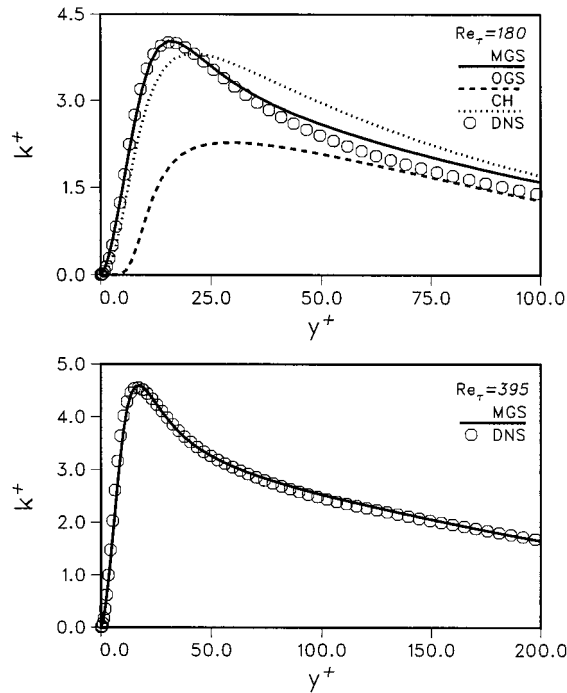


Figure 6. Turbulence kinetic energy profiles of channel flow.

are made by J. Coupland at Rolls Royce. The inlet velocity is 9.4 m s^{-1} and the pressure gradient is zero. The upstream turbulence intensity $Tu = 6.0$ per cent, defined as $Tu = \sqrt{2/3k}/U_{\text{ref}}$, where U_{ref} indicates the reference velocity. The dissipation is set so that the decay of free-stream turbulence is in balance.

Computations begin 16 cm ahead of the leading edge and symmetric conditions are applied. The length and height of the grid are 1.6 and 0.3 m respectively. The near-wall node is located at $y^+ < 1.0$, except the point at the leading edge ($y^+ = 2.1$). The grid size is 96×64 and heavily clustered near the wall.

The predicted skin friction coefficients ($C_f = 2u_{\tau}^2/U_{\text{ref}}^2$) are compared with the experimental data in Figure 8. The overall performance in predicting the friction coefficient is the best for the OGS model, exhibiting an interesting feature that the transition starts at the right position, although it is not strong enough. Seemingly, the CH model gives earlier transition than that seen in the experiment, and it is too weak. In contrast, the MGS model predicts an overshoot following the transition in line with the experiment, and after the transition, it gives values of C_f that agree well with the fully turbulent line.

Profiles of the mean velocity are shown in Figure 9 at four representative positions. The OGS model predicts the laminar profile near the leading edge of the flat plate, whereas the MGS model is turbulent all the way down, as is clearly noticed from the figure. However, the

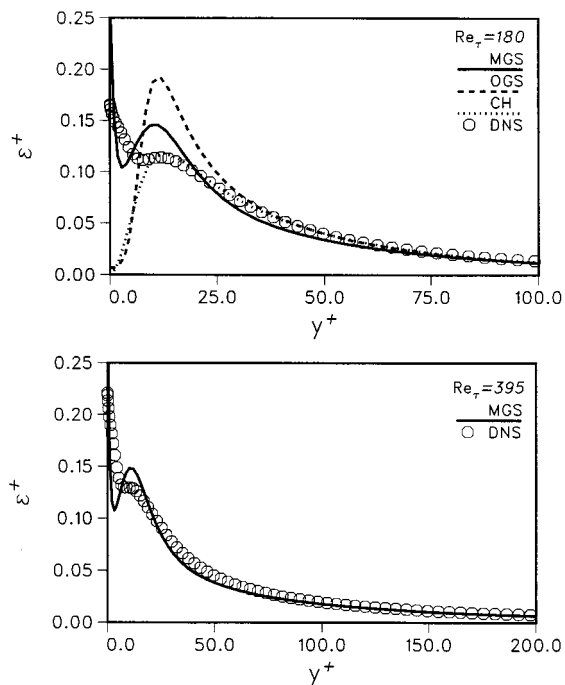


Figure 7. Dissipation rate profiles of channel flow.

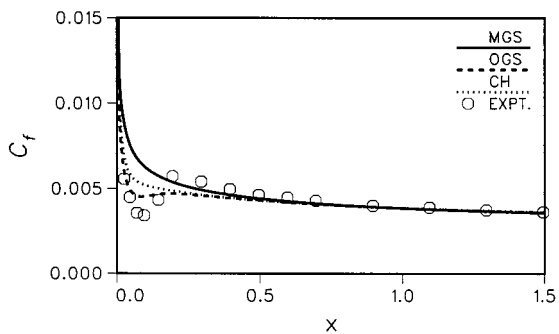


Figure 8. Streamwise variations of the skin friction coefficient.

agreement between the calculations and the experiments is fairly good toward the end of the transition (e.g., beyond $x = 0.195$ m). The distribution of the turbulence intensities is depicted in Figure 10. As is observed, predictions of all models are somewhat on a lower level than the data show, especially in the region $5 < y^+ < 70$.

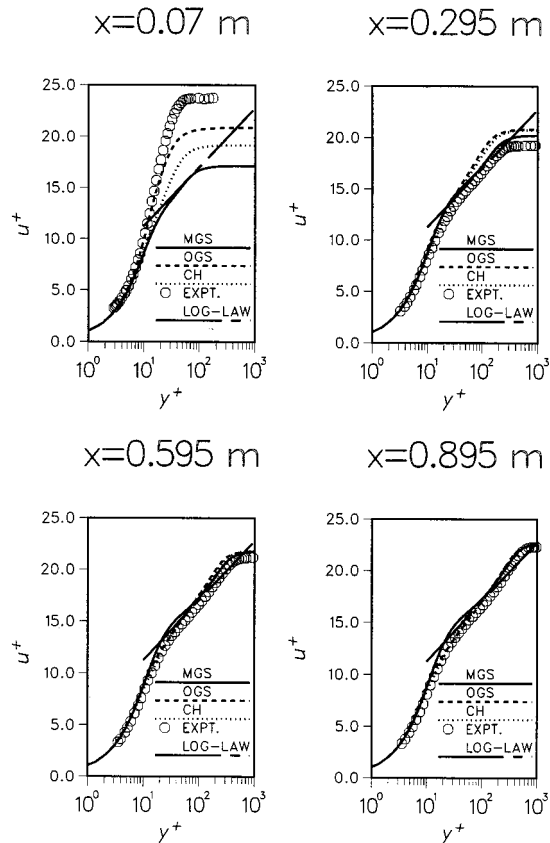


Figure 9. Mean velocity profiles at different downstream stations.

4.3. Backward-facing step flow

To validate the performance in complex separated and reattaching turbulent flows, the MGS model is applied to the flow over a backward-facing step. The computations are conducted corresponding to the experimental case with zero deflection of the wall opposite to the step, as investigated by Driver and Seigmiller [30]. The reference velocity $U_{\text{ref}} = 44.2 \text{ m s}^{-1}$ and the step height $h = 0.0127 \text{ m}$. The ratio between the channel height and the step height is 9, and the step height Reynolds number is $Re = 37500$. At the channel inlet, the Reynolds number based on the momentum thickness is $Re_{\theta} = 50000$.

For the computations, grids are arranged in two blocks. The smaller one (extended from the inlet to the step) contains a 16×48 non-uniform grid and the grid size for other one is 120×80 . The inlet conditions are specified four step heights upstream of the step corner and

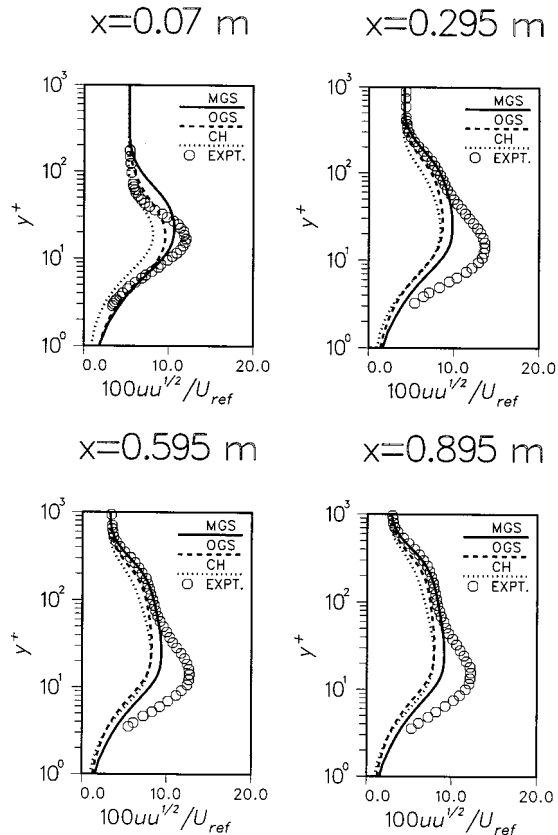


Figure 10. Turbulent intensity profiles at different downstream stations.

the outlet boundary conditions are imposed 30 step heights downstream of the step corner. The inlet profiles for all dependent variables are generated by solving the models at the appropriate momentum thickness Reynolds number. All the quantities shown below are normalized by the step height h and the experimental reference free-stream velocity U_{ref} , provided that the distance x/h is measured exactly from the step corner.

Computed and experimental friction coefficients C_f along the bottom wall (step side wall) are plotted in Figure 11. As is observed, the CH model gives the C_f distribution with a large overshoot followed by a sudden drop in the immediate vicinity of the reattachment point. The MGS model predicts the skin friction coefficient qualitatively. The positive C_f that starts from $x/h = 0$, is due to a secondary eddy, which sits in the corner at the base of the step, inside the main recirculation region. The recirculation length predicted by each model can be determined by measuring the distance from the step corner to a point at which the curve changes sign. The

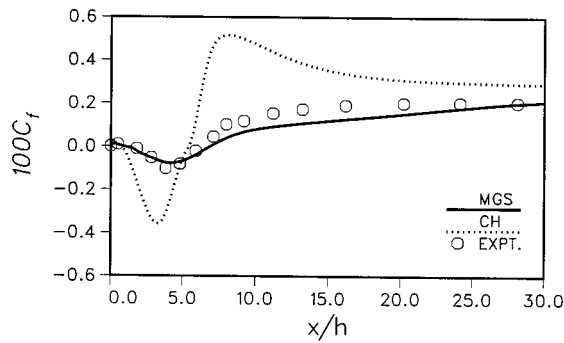


Figure 11. Skin friction coefficient along the step-side bottom wall.

CH model predicts a recirculation length of 5.4, and the corresponding prediction by the MGS model is 6.8. The experimental value of the reattachment length is 6.26 ± 0.1 , making a fairly good correspondence with the MGS model.

In Figure 12, the streamwise mean velocity profiles predicted by both the CH and MGS models are compared with the experimental data. Obviously, the predictions of both models are in good agreement with the experiment. It is a bit nebulous that the inaccurate prediction of the C_f distribution by the CH model has little effect on the u -profiles.

Comparisons are extended to the distributions of the turbulent kinetic energy and the corresponding Reynolds shear stress at different x/h locations behind the step corner, as shown in Figures 13 and 14. Since the w component is not measured in the experiment, the usual approximation $k \approx 3/4(\overline{uu} + \overline{vv})$ is employed. A closer inspection of the distribution indicates that the MGS model predictions are in a broad agreement with the experimental data. The agreement is better in the recirculation region rather than in the recovery region. It seems likely that this is a common feature of turbulent flows with separation and reattachment [31].

4.4. Semi-confined impinging slot jet

The single jet configuration with $H/W = 1.5$ (where W is the jet width and H is the distance between the nozzle and the impingement surface), as studied experimentally by Ichimiya and Hosaka [32], is considered. The Reynolds number based on the slot width is 8000, and the length of the computational domain is chosen to be 20 times the jet width. An 80×48 grid is placed non-uniformly in the computational domain. The boundary conditions are given in Reference [8].

Figure 15 compares the predicted Nusselt number with that of the experiment. The distance from the symmetric axis is normalized by half of the jet width. As can be seen, predictions of the MGS model agree well with the experiment.

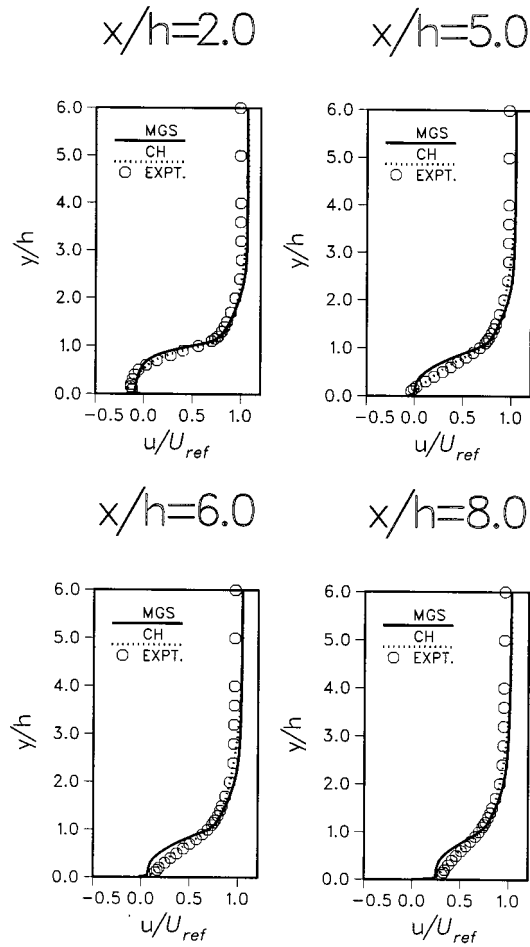


Figure 12. Mean velocity profiles at selected locations for backward-facing step flow.

4.5. Semi-confined impinging axisymmetric jet

The performance of the proposed model is further contrasted with the experimental data of the turbulent axisymmetric jet impinging within a semi-confined space [33]. The Reynolds number based on the nozzle diameter D is 20000 and a nozzle to plate space is of $2D$. A uniform velocity is specified at the inlet, and the inlet profiles for the turbulent kinetic energy and energy dissipation are evaluated from $k = 0.003U_{ref}^2$ and $\epsilon = 3k^{1.5}/(D/2)$ respectively. A

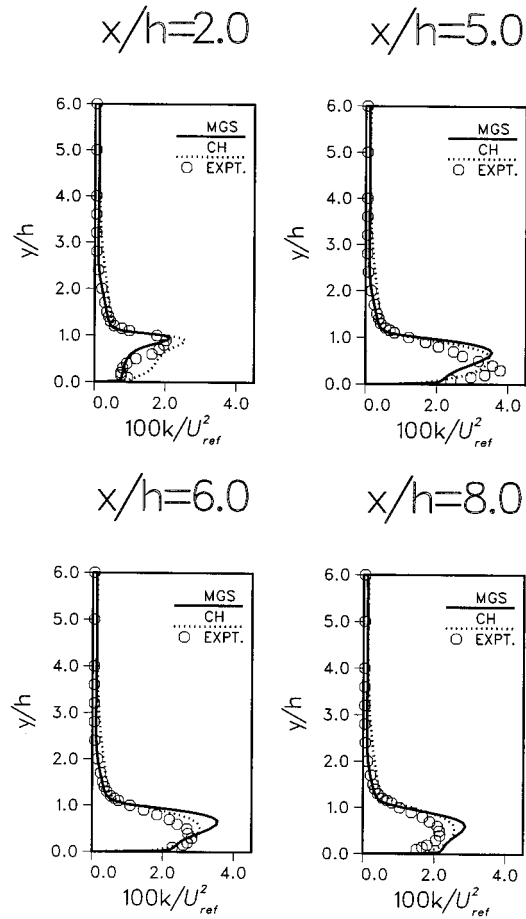


Figure 13. Kinetic energy profiles at selected locations for backward-facing step flow.

constant temperature is prescribed at the wall, which simulates the experimental boundary condition [33]. An 80×48 grid is adopted with a heavy clustering near the wall.

Figure 16 displays the comparison of the predicted Nusselt number with the experiment. The distance from the symmetric axis is normalized by the diameter of the jet. As is evident, the MGS model overpredicts Nu by about 70 per cent at the stagnation point. The inability of the numerical model to predict the heat transfer coefficient in the stagnation region may be attributed to the isotropic nature of the turbulent heat flux modeling.

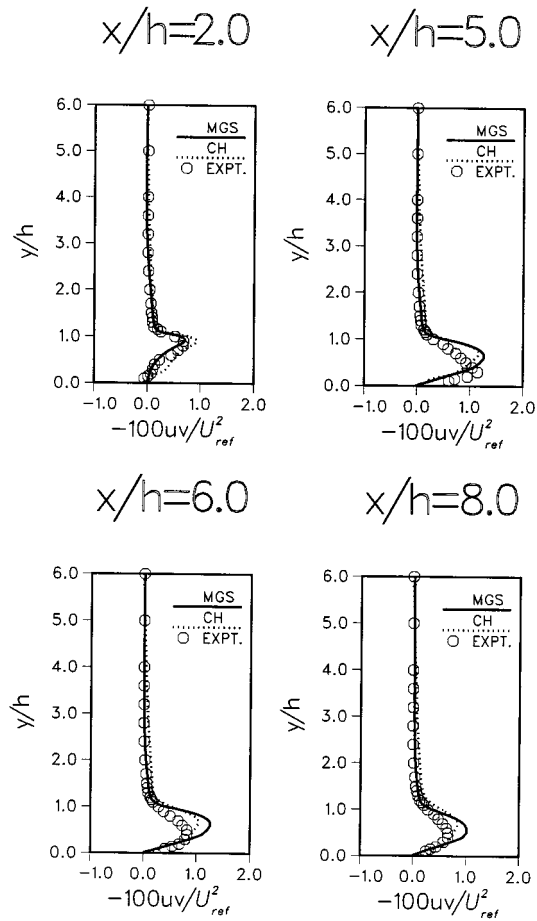


Figure 14. Shear stress profiles at selected locations for backward-facing step flow.

5. CONCLUSIONS

The MGS model accounts for the near-wall and low-Reynolds number effects originating from the physical requirements. The modified strain-dependent coefficients alleviate the numerical instabilities as is experienced by the OGS model. The modified constant $C_{\epsilon 1}$ and a secondary positive source term in the dissipation equation enhance dissipation in near-wall regions. It enforces the realizability constraints. The new model invokes a simple wall-boundary condition for ϵ . Comparisons of the model predictions with the experimental and DNS data for well-documented flows demonstrate that the MGS model offers considerable improvement over the OGS model.

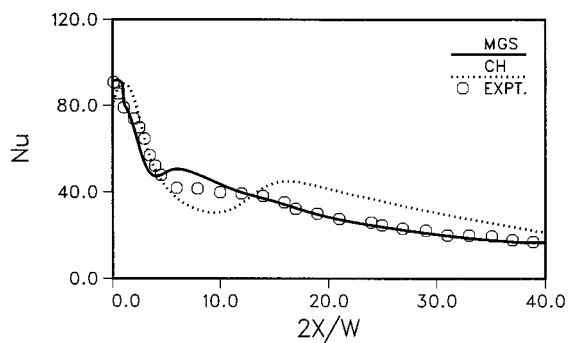


Figure 15. Nusselt number distribution on the impingement wall for slot jet.

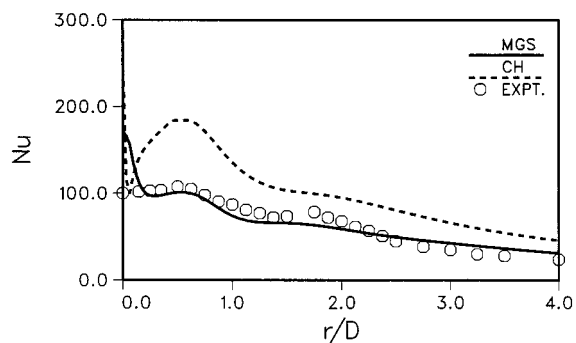


Figure 16. Nusselt number distribution on the impingement wall for round jet.

APPENDIX A. NOMENCLATURE

b_{ij}	Reynolds stress anisotropy
C_f	friction coefficient
C_μ	eddy viscosity coefficient for Gatski and Speziale model
C_μ^*	eddy viscosity coefficient for modified Gatski and Speziale model
D	diameter of a round jet
e	specific internal energy
E	total internal energy; source term in dissipation equation
F, G	flux vectors in x -, y -direction
h	step height
\vec{i}, \vec{j}	unit vectors in Cartesian co-ordinate system
k	turbulent kinetic energy; heat conductivity
Nu	local Nusselt number
p	static pressure

P	production of turbulent kinetic energy
Pr	Prandtl number
q	heat flux
Q	source term
S	mean strain rate
t	time
T	temperature
u, v	velocity components in the x -, y -directions
U	vector of conservative variables
W	slot width; mean vorticity
x, y	Cartesian co-ordinates
y^+	non-dimensional normal distance from the surface

Greek letters

δ	half-width of a channel
δ_{ij}	Kronecker's delta
ϵ	dissipation of turbulent kinetic energy
μ	dynamic viscosity
ν	kinematic viscosity
ρ	density
σ	Schmidt's number
τ	shear stress

Subscripts

T	turbulent condition
ref	reference condition
v	viscous part

REFERENCES

1. Rodi W. A new algebraic relation for calculating the Reynolds stresses. *Z Angew Mathematics and Mechanics* 1976; **56**: T219–221.
2. Pope SB. A more general effective viscosity hypothesis. *Journal of Fluid Mechanics* 1975; **72**: 331–340.
3. Launder BE, Reece G, Rodi W. Progress in the development of a Reynolds stress closure. *Journal of Fluid Mechanics* 1975; **68**: 537–566.
4. Gatski TB, Speziale CG. On the explicit algebraic stress models for complex turbulent flows. *Journal of Fluid Mechanics* 1993; **254**: 59–78.
5. Lumley JL. Computational modeling of turbulent flows. *Advances in Applied Mechanics* 1978; **18**: 124–176.
6. Abid R, Rumsey C, Gatski TB. Prediction of nonequilibrium turbulent flows with explicit algebraic stress models. *AIAA Journal* 1995; **33**: 2026–2031.
7. Abid R, Morrison JH, Gatski TB, Speziale CG. Prediction of aerodynamic flows with a new explicit algebraic stress model. *AIAA Journal* 1997; **34**: 2632–2635.

8. Rahman MM, Rautahaimo P, Siikonen T. Numerical study of turbulent heat transfer from a confined impinging jet using a pseudo-compressibility method. In *Second International Symposium on Turbulence, Heat and Mass Transfer*, Delft, The Netherlands, Hanjalic K, Peeters TWJ (eds). Delft University Press: Delft, 1997; 511–520.
9. Tavoularis S, Corrsin A. Experiments in nearly homogeneous turbulent shear flow with a uniform mean temperature gradient. Part I. *Journal of Fluid Mechanics* 1981; **104**: 311–347.
10. Durbin PA. Near-wall turbulence closure modeling without damping functions. *Theoretical Computational Fluid Dynamics* 1991; **3**: 1–13.
11. Goldberg U. Derivation and testing of a one-equation model based on two time scales. *AIAA Journal* 1993; **31**: 1191–1198.
12. Yang Z, Shih TH. New time scale based k - ϵ model for near-wall turbulence. *AIAA Journal* 1991; **29**: 1337–1340.
13. Goldberg U, Apsley D. A wall-distance-free low Re k - ϵ turbulence model. *Computer Methods in Applied Mechanics and Engineering* 1997; **145**: 227–238.
14. Durbin PA, Speziale CG. Local anisotropy in strained at high Reynolds numbers. *Journal of Fluids Engineering* 1991; **113**: 707–709.
15. Mansour NN, Kim J, Moin P. Near-wall k - ϵ turbulence modeling. *AIAA Journal* 1989; **27**: 1068–1073.
16. Yap CR. Turbulent heat and momentum transfer in recirculating and impinging flows. PhD thesis, Faculty of Technology, University of Manchester, 1987.
17. Durbin PA. A Reynolds-stress model for near-wall turbulence. *Journal of Fluid Mechanics* 1993; **249**: 465–498.
18. Laurence D, Parneix S, Durbin PA. Second moment closure analysis of a DNS backstep flow database. In *Second International Symposium on Turbulence, Heat and Mass Transfer*, Delft, The Netherlands, Hanjalic K, Peeters TWJ (eds). Delft University Press: Delft, 1997; 341–350.
19. Craft TJ, Launder BE, Suga K. Prediction of turbulent transitional phenomena with a nonlinear eddy-viscosity model. *International Journal of Heat and Fluid Flow* 1997; **18**: 15–28.
20. Patel VC, Rodi W, Scheuerer G. Turbulence models for near-wall and low Reynolds number flows: a review. *AIAA Journal* 1985; **23**: 1308–1319.
21. Kim J, Moin P, Moser R. Turbulence statistics in fully developed channel flow at low Reynolds number. *Journal of Fluid Mechanics* 1987; **177**: 133–166.
22. Mansour NN, Kim J, Moin P. Reynolds-stress and dissipation-rate budgets in a turbulent channel flow. *Journal of Fluid Mechanics* 1988; **194**: 15–44.
23. Antonia RA, Kim J. Low-Reynolds number effects on near-wall turbulence. *Journal of Fluid Mechanics* 1994; **276**: 61–80.
24. Roe PL. Approximate Riemann solvers, parameter vectors, and difference schemes. *Journal of Computational Physics* 1981; **43**: 357–372.
25. Lombard C, Bardina J, Venkatapathy E, Olinger J. Multi-dimensional formulation of CSCM-an upwind flux difference eigenvector split method for the compressible Navier–Stokes equations. In *Sixth AIAA Computational Fluid Dynamics Conference*, AIAA Paper 83-1895-CP, 1983; 649–664.
26. Jameson A, Yoon S. Multigrid solution of the Euler equations using implicit schemes. *AIAA Journal* 1986; **24**: 1737–1743.
27. Rautahaimo P, Siikonen T. Implementation of the Reynolds stress turbulence model. In *Third ECCOMAS Computational Fluid Dynamic Conference*, Paris, Desideri JA, Hirsch C, LeTallec P, Pandolfi M, Periaux J (eds). Wiley: Chichester, 1996; 352–358.
28. Siikonen T. An application of Roe's flux-difference splitting for k - ϵ turbulence model. *International Journal for Numerical Methods in Fluids* 1995; **21**: 1017–1039.
29. Chien K-Y. Predictions of channel and boundary layer flows with a low-Reynolds number turbulence model. *AIAA Journal* 1982; **20**: 33–38.
30. Driver DM, Seigmiller HL. Features of a reattaching turbulent shear layer in divergent channel flow. *AIAA Journal* 1985; **23**: 163–171.
31. So RMC, Lai YG, Yoo GJ. Low-Reynolds number modeling of flows over a backward-facing step. *Journal of Applied Mathematical Physics* 1988; **39**: 13–27.
32. Ichimiya K, Hosaka N. Experimental study of heat transfer characteristics due to confined impinging two-dimensional jets (heat transfer experiment for three slot jets). *Transactions of the Japanese Society of Mechanical Engineers Part B* 1989; **55**: 3210–3215.
33. Ashforth-Frost S, Jambunathan K. Numerical prediction of semi-confined jet impingement and comparison with experiment. *International Journal for Numerical Methods in Fluids* 1996; **23**: 295–306.